The Inner and Outer Shock Layers of Bow Shocks in Cataclysmic Variables

The Astrophysical Journal Letters, 1000:L22 (10pp), 2026 March 20 https://doi.org/10.3847/2041-8213/ae4aa7

The Inner and Outer Shock Layers of Bow Shocks in Cataclysmic Variables

Krystian Iłkiewicz[1], Christian Knigge[2], Simone Scaringi[3,4], Noel Castro Segura[5], Santiago del Palacio[6], and Martina Veresvarska[7,8]

[1] Nicolaus Copernicus Astronomical Center, Polish Academy of Sciences, Bartycka 18, 00-716 Warsaw, Poland; ilkiewicz@camk.edu.pl
[2] School of Physics and Astronomy, University of Southampton, Highfield, Southampton SO17 1BJ, UK
[3] Centre for Extragalactic Astronomy, Department of Physics, Durham University, DH1 3LE, UK
[4] INAF-Osservatorio Astronomico di Capodimonte, Salita Moiariello 16, I-80131 Naples, Italy
[5] Astronomy and Astrophysics Group, Department of Physics, University of Warwick, Coventry CV4 7AL, UK
[6] Department of Space, Earth and Environment, Chalmers University of Technology, SE-412 96 Gothenburg, Sweden
[7] Institute of Space Sciences (ICE, CSIC), Campus UAB, Carrer de Can Magrans s/n, 08193, Barcelona, Spain
[8] Institut d'Estudis Espacials de Catalunya (IEEC), Esteve Terradas 1, RDIT Building, 08860, Castelldefels, Spain
Received 2026 January 27; revised 2026 February 19; accepted 2026 February 24; published 2026 March 16

Abstract

Bow shocks around cataclysmic variables (CVs) have traditionally been identified with a single bright optical arc. This feature has been interpreted as the bow shock formed by the interaction between a sustained outflow and the interstellar medium (ISM). We show that this interpretation is incomplete. Generic wind–ISM interaction theory predicts a two-shock configuration consisting of an inner terminal wind (reverse) shock and an outer forward shock, separated by a hot, low-density shocked wind cavity. Using archival ultraviolet, optical, and infrared imaging of the nova-like systems BZ Cam and V341 Ara, and the polar 1RXS J052832.5+283824, we find that the nebulae around all three systems exhibit this layered structure. In each case, the previously identified bow shock bright in Hα and [O III] corresponds to a compact inner arc, while additional emission components reveal a more extended morphology. Specifically, each system shows an outer arc detected in mid-infrared images, and the region between the optical and infrared arcs is filled with faint Hα emission and, where available, far-ultraviolet emission. We identify this infrared arc, reported here for the first time in these systems, as the sweep-up boundary of the forward shock, while the bright inner optical arc corresponds to the terminal wind shock rather than the forward shock as previously assumed. These results reveal that the true extent and layered structure of bow shocks around CVs only become apparent when observations extend beyond the optical band.

Unified Astronomy Thesaurus concepts: Cataclysmic variable stars (203); Stellar bow shocks (1586); Stellar winds (1636); Interstellar medium (847); AGN host galaxies (2017); Ultraviolet astronomy (1736); Infrared astronomy (786)

1. Introduction

Cataclysmic variables (CVs) are close interacting binaries in which a late-type donor transfers mass to a white dwarf (WD). The accretion geometry is set largely by the WD magnetic field: weakly magnetic systems form an accretion disk, intermediate polars host truncated disks with magnetically controlled accretion curtains, and polars channel the flow directly along field lines onto the WD poles. Some CVs, and in particular high-mass-transfer nova-like systems, also launch sustained outflows. These winds are most clearly revealed through P Cygni profiles of emission lines in the ultraviolet (UV) and optical range, indicating mass loss with characteristic velocities of order a few 10^2–10^3 km s^{-1} (e.g., J. M. Hollis et al. 1992; J. Greiner et al. 2001).

When a source with a sustained outflow moves through the interstellar medium (ISM), the wind–ISM interaction can produce a bow shock. Persistent, spatially resolved bow shocks have been identified around only a handful of CVs to date (e.g., J. Krautter et al. 1987; H. E. Bond & B. Miszalski 2018; J. V. Hernández Santisteban et al. 2019; H. E. Bond et al. 2025; K. Iłkiewicz et al. 2026), but those systems provide direct constraints on the long-term momentum and energy input from compact binaries into their local environments (N. Castro Segura et al. 2021; K. Iłkiewicz et al. 2026).

BZ Cam is nova like with the best-studied bow shock among CVs. The BZ Cam bow shock is often portrayed as dominated by a single bright optical arc seen in Hα and [O III], a feature that has been interpreted as the forward shock or H II front produced by the wind–ISM interaction (J. M. Hollis et al. 1992). Subsequent work, however, has shown that the bow-shock morphology and excitation are more complex than this single-layer picture implies. Namely, deeper imaging and kinematic studies reveal extended, asymmetric structure, and spatially varying ionization that are not easily reconciled with a single, steady forward shock (J. Greiner et al. 2001). Moreover, theoretically idealized wind–ISM interactions produce a two-shock geometry consisting of an inner reverse/terminal shock that decelerates and heats the fast outflow and an outer forward shock that sweeps up and compresses the ambient medium, with a large hot shocked-wind cavity between them (J. M. Hollis et al. 1992). These regions differ by few orders of magnitude in density and temperature, so their observational signatures can be very different. As a result, mapping these theoretical zones to observational tracers is nontrivial, and multiwavelength imaging is required to disentangle terminal-shock, forward-shock, and photoionized components.

In this work we test whether CV bow shocks display the generic two-shock wind–ISM structure. We focus on the three

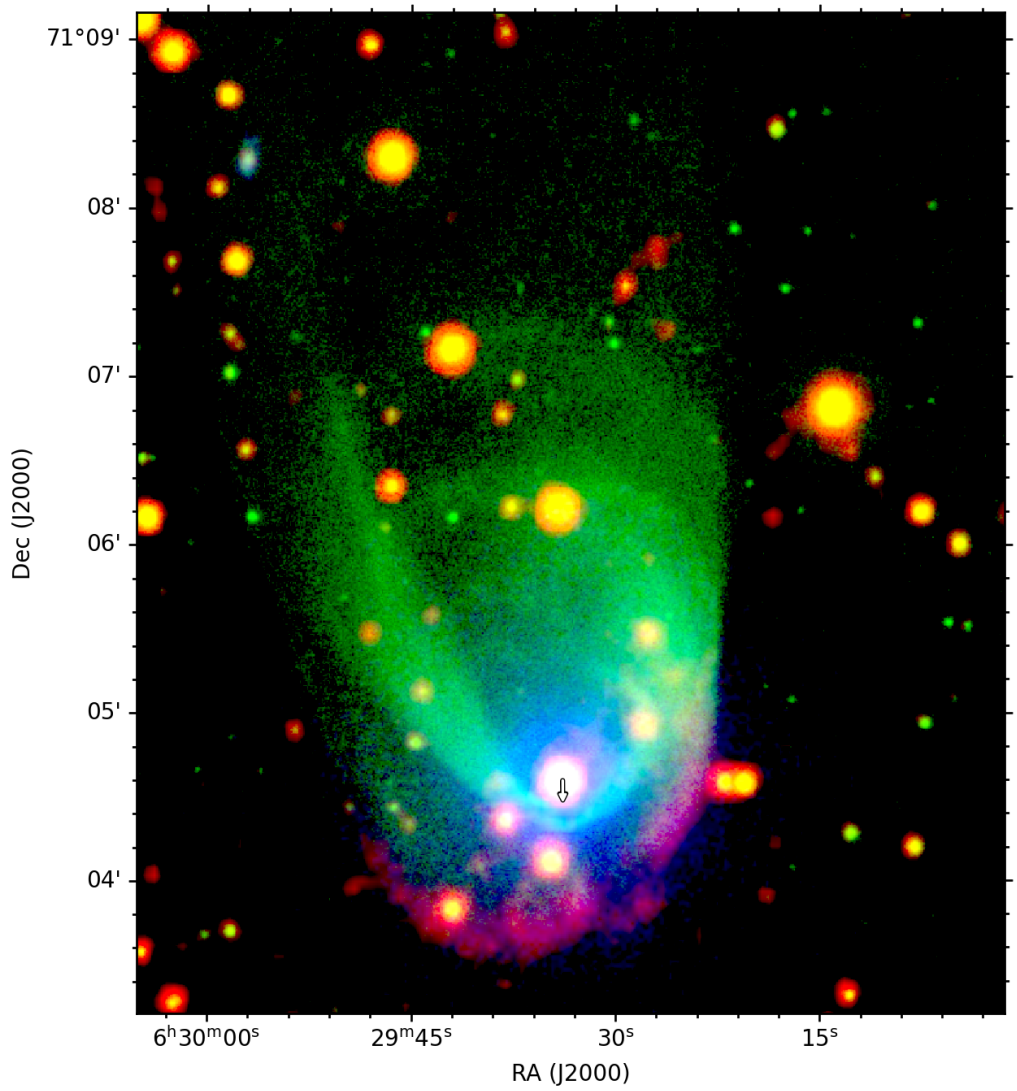

Figure 1. False-color composite image of BZ Cam: GALEX FUV (blue), Hα (green; H. E. Bond & B. Miszalski 2018), and unWISE W2 (red). The morphology is stratified: a compact inner optical bow shock, an extended FUV/faint Hα interior, and an outermost W2 shell. The arrow indicates the Gaia proper-motion vector (Gaia Collaboration et al. 2023) corrected for Galactic rotation. The corrected proper motion is (μ_α, μ_δ) = (–0.69 ± 0.02, –21.61 ± 0.07) mas yr^{-1}. The corresponding tangential, radial, and total space velocities are $V_t = 38.4 \pm 0.4$ km s^{-1}, $V_r = -69 \pm 10$ km s^{-1}, and $V = 79.3 \pm 8.8$ km s^{-1}. North is up, east is left.

best-characterized systems: nova-like systems BZ Cam and V341 Ara and the diskless polar 1RXS J052832.5+283824 (RXJ0528+2838). We combine archival UV and infrared imaging with published narrowband Hα and [O III] maps. By comparing the spatial distributions of emission across these wavelength regimes, we assess how different observational tracers relate to the underlying shock structure and evaluate whether the commonly adopted single-layer interpretation of CV bow shocks provides a complete description. This approach allows us to place the observed nebulae in the broader context of wind-driven bow shocks.

2. Data Selection

We searched archival images for bow shocks associated with BZ Cam, V341 Ara, and RXJ0528+2838 using survey data accessible through the Centre de Données astronomiques de Strasbourg Virtual Observatory services (F. Bonnarel et al. 2000). For each target, we inspected all available survey observations and selected the datasets offering new insights into the structure of the bow shocks.

The bow shock of BZ Cam is detected in the far-ultraviolet (FUV; 1350–1750 Å) but not at the longer wavelengths covered by the near-ultraviolet (NUV) detectors (1750–2800 Å) of the Galaxy Evolution Explorer (GALEX; P. Morrissey et al. 2007). This UV bow shock was previously reported in Swift observations by P. Zemko et al. (2014) but was not analyzed in detail. We note that the UV ring-like feature reported by P. Zemko et al. (2014) in the UVOT image is located at a larger off-axis angle than the CV, consistent with known UVOT ghost artifacts. The corresponding UVOT quality map produced with `uvotflagqual` flags this region, and no counterpart is detected in our GALEX data. Together, these facts indicate that the ring is an instrumental artifact. For V341 Ara, no FUV observations are available, and as in BZ Cam, no bow-shock features are detected in the NUV images. For RXJ0528+2838, no GALEX observations exist.

In the infrared the BZ Cam bow shock is visible in Unblurred Coadds of the WISE (unWISE; D. Lang 2014)

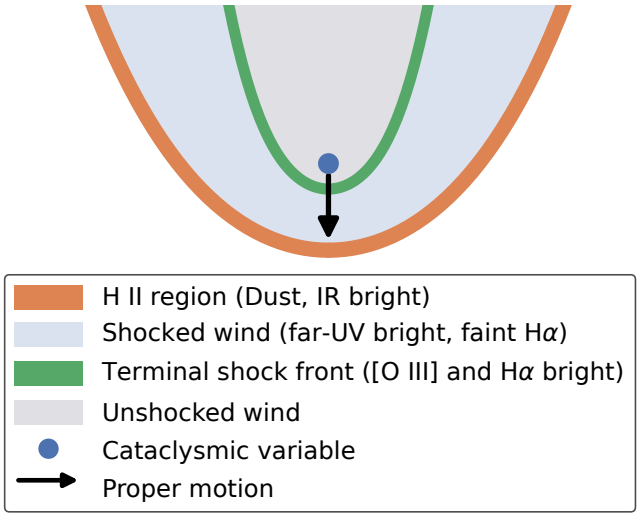

Figure 2. Schematic mapping between observed tracers and physical zones in the two-shock interpretation of CV bow shocks. The outermost layer (orange) represents the swept-up H II/forward-shock boundary traced by infrared-emitting dust. The inner bow shock (green) represents the terminal/reverse shock front, which is bright in [O III] and Hα. The region between the two bow shocks (blue) is the shocked-wind cavity expected to be bright in the FUV and only faintly in Hα. The inner region (gray) indicates unshocked wind with no clear observational signatures. The arrow shows the CV proper-motion direction.

longer wavelength W2 images (3.96–5.34 μm) but not in the shorter wavelength W1 band images (2.75–3.87 μm). The bow shocks of RXJ0528+2838 and V341 Ara are also present in W2, though their detailed morphology is harder to analyze because of the relatively low spatial resolution of the Wide-field Infrared Survey Explorer (WISE). Specifically, in V341 Ara the bow shock is less pronounced due to strong crowding in the field, while in RXJ0528+2838 the nebula is partially blended with the nearby bright infrared source 2MASS J05283260+2837556.

To increase the visibility of the bow shocks in RXJ0528 +2838 and V341 Ara, we scaled the W1 images to match the mean stellar brightness in W2 and subtracted W1 from W2, thereby removing most of the stellar contamination. We note that because the W2 point-spread function is larger than that in W1, this procedure introduces residual artifacts in the form of rings at the locations of bright stars.

The optical narrowband images of BZ Cam are taken from H. E. Bond & B. Miszalski (2018), for V341 Ara from N. Castro Segura et al. (2021), and for RXJ0528+2838 from K. Iłkiewicz et al. (2026).

3. Results: Layered Bow-shock Morphology

3.1. BZ Cam: The Predicted Two-shock Stratification

Figure 1 compares the FUV, Hα, and W2 morphologies of BZ Cam bow shock. The emission is clearly stratified into three spatially distinct components.

(i) Inner optical bow shock. The compact bow-shaped arc bright in Hα and [O III] λ5007 lies closest to the CV. This structure corresponds to the bow shock discussed in previous optical studies and has historically been treated as the primary manifestation of the wind–ISM interaction (e.g., J. M. Hollis et al. 1992; J. Greiner et al. 2001).

(ii) Intermediate faint layer. Beyond the bright optical arc, a broader emission region bright in FUV is visible, which seems to be accompanied by a fainter Hα component. This extended component is consistent with emission from hot, low-density gas and/or strong FUV lines commonly associated with shocked winds (e.g., C IV, He II, N V), although spectroscopy is required to determine the dominant contributors. This more extended Hα emission is clearly visible in previous publications, though it has not been explicitly discussed by the authors (e.g., J. Greiner et al. 2001).

(iii) Outer dust bow. The most extended structure detected in W2 defines the outer edge of a larger bow shock. The W2 bow shock extends to $\sim$55″, much larger than the $\sim$15″ bright optical arc. The appearance in W2 and not W1 indicates cool dust emission concentrated near the swept-up boundary. Although the infrared bow axis remains aligned with the proper motion of BZ Cam, the infrared morphology appears more asymmetric than that of the inner optical bow shock, with the infrared bow apex shifted farther east of the CV proper motion.

This ordering, with a high-ionization optical bow shock inside, FUV emission filling the cavity, and an outer infrared rim, is consistent with theoretical models of wind–ISM interactions, provided that the bright inner optical arc is associated with the terminal-wind (reverse) shock or with photoionized wind material immediately upstream of the terminal shock. In this interpretation, the outer infrared shell traces the forward shock propagating into the ISM and the associated compressed, swept-up dust layer (i.e., the H II region/forward shock). A schematic mapping between the observed tracers and the physical zones of the BZ Cam bow shock is shown in Figure 2. The observed asymmetry of the infrared bow shock likely reflects inhomogeneities in the local ISM, with the bow-shock surface expanding preferentially toward regions of lower external ram pressure (e.g., M. V. Barkov et al. 2019). In this interpretation, the eastward displacement of the infrared apex relative to the direction of proper motion implies a lower ISM density toward the southeast than toward the southwest, although asymmetry in the outflow cannot be ruled out. The differing asymmetries observed in the infrared and optical bow shocks may arise because infrared emission traces dust near the outer boundary of the interaction region, where coupling to the large-scale ISM is strongest, whereas Hα and [O III] emission originate closer to the CV, where the flow is partially shielded from ISM density variations by the forward shock.

The infrared bow shock exhibits a somewhat clumpy morphology. Several of the brightest knots correspond to sources in the WISE All-Sky Source Catalog (WISEA), each with a unique identifier (e.g., WISEA J062924.50+710430.7). Using the catalog photometry (R. M. Cutri et al. 2021), we identified 11 such clumps with no clear optical counterparts, of which 4 have measurements in the W1, W2, and W3 bands and only upper limits in W4, while the remaining 7 knots are detected only in W1 and W2.

For the four clumps with three-band detections, we fitted simple blackbody models to their spectral energy distributions (SEDs), obtaining dust temperatures of $\sim$500–600 K (see the Appendix). Because the SEDs are constrained by only three photometric points, the blackbody fits should be interpreted with caution and are intended primarily to demonstrate the presence of warm dust rather than to characterize the detailed nature of the mid-infrared emission. These temperatures are nevertheless similar to those inferred at the apices of bow

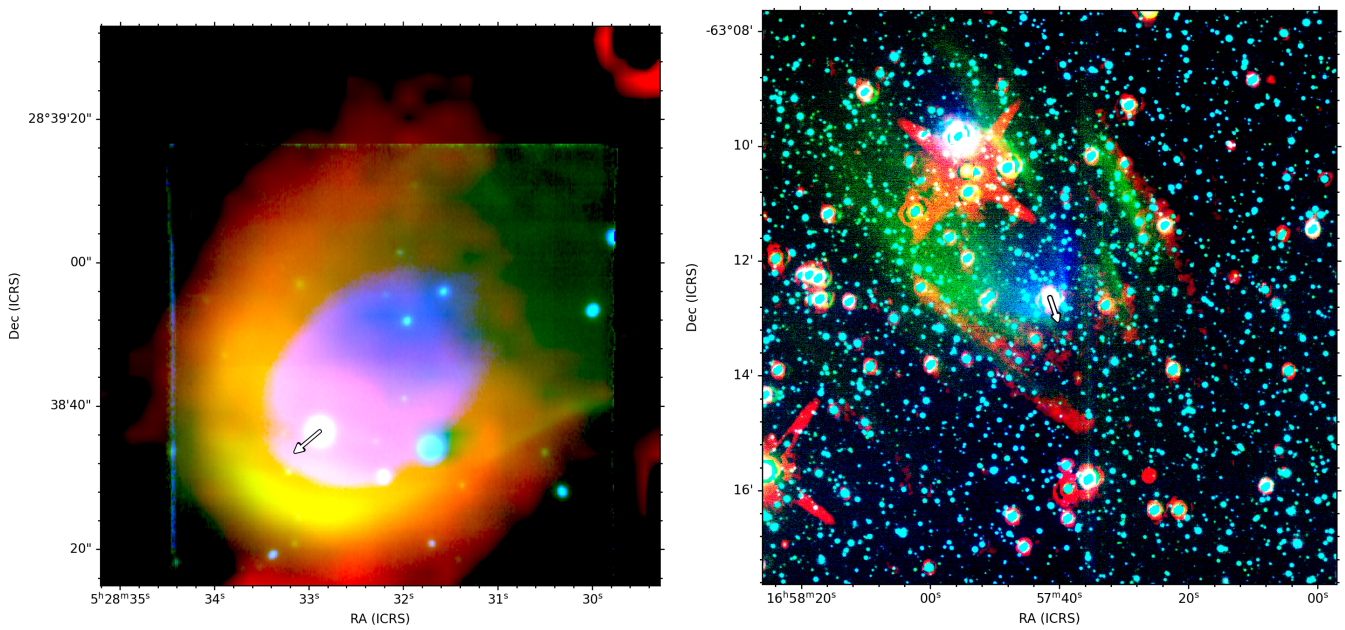

Figure 3. False-color images of RXJ0528+2838 (top) and V341 Ara (bottom). Blue: [O III] λ5007; green: Hα; red: W2 – W1 difference (to suppress stellar crowding; see the text). Optical narrowband images are from K. Ikiewicz et al. (2026; RXJ0528+2838) and N. Castro Segura et al. (2021; V341 Ara). In both systems, the infrared emission marks the outermost bow-shock layer. The arrows indicate the Gaia proper-motion vectors (Gaia Collaboration et al. 2023) corrected for Galactic rotation. For RXJ0528+2838, the corrected proper motion is (μ_α, μ_δ) = (39.31 $\pm$ 0.06, –29.1 $\pm$ 0.2) mas yr^{-1}, corresponding to V_t = 52.2 $\pm$ 0.9 km s^{-1}, V_r = 117.4 $\pm$ 5.0 km s^{-1}, and a total space velocity V = 128.5 $\pm$ 4.6 km s^{-1}. For V341 Ara, the corrected proper motion is (μ_α, μ_δ) = (–44.89 $\pm$ 0.03, –60.2 $\pm$ 0.1) mas yr^{-1}, with V_t = 55.5 $\pm$ 0.4 km s^{-1}, V_r = 47.1 $\pm$ 2.0 km s^{-1}, and V = 72.7 $\pm$ 1.3 km s^{-1}. North is up, east is left.

shocks around massive stars (J. Sanchez-Bermudez et al. 2014), where dust is heated by a combination of radiative and shock-related processes. In the case of BZ Cam, the dust is unlikely to be heated predominantly by radiation from the CV given its relatively low luminosity and the large bow-shock standoff distance and is more likely heated by irradiation from shock-generated UV photons. However, more detailed observations will be required before firm conclusions can be drawn regarding the dominant dust heating mechanism.

We also extracted WISE multiepoch photometry for the clumps in the W1 and W2 bands using the procedures of H.-C. Hwang & N. L. Zakamska (2020).[9] None of the clumps shows statistically significant variability, although the photometric uncertainties are large.

3.2. RXJ0528+2838 and V341 Ara: The Same Stratification across Accretion Regimes

In contrast to BZ Cam, RXJ0528+2838 and V341 Ara lack FUV imaging, and their infrared observations provide more limited constraints on the bow-shock structure. In RXJ0528 +2838 the nebula is compact and only marginally resolved, while in V341 Ara strong stellar crowding reduces the contrast of the infrared emission. As a result, we do not recover the same level of morphological detail as in BZ Cam. Nevertheless, both RXJ0528+2838 and V341 Ara exhibit clear infrared bow-shock emission in the unWISE W2 data (Figure 3), which traces cool dust at the outermost extent of their nebulae.

In RXJ0528+2838, the W2 emission forms a well-defined parabolic arc that follows the outer boundary of the optical bow shock. Although the small angular size of the nebula (~16.″8) limits the amount of detail that can be recovered at the WISE resolution (~6″), the infrared arc is aligned with the system proper motion and reproduces the overall shape of the Hα emission. The [O III] bow shock is confined to a smaller region interior to the W2 rim.

V341 Ara exhibits an analogous configuration on a larger angular scale. The W2 emission appears as an incomplete arc along the outer edge of the extended Hα nebula previously discussed as a possible remnant nova shell (N. Castro Segura et al. 2021). As in RXJ0528+2838, the infrared arc coincides with the outer boundary of the faint Hα emission, while the [O III] emission highlights more internal, higher ionization structure. This morphology with outer infrared rim suggests that the larger Hα structure is not a nova shell but instead traces a shocked-wind cavity similar to that seen in BZ Cam. However, we note that a nova shell interpretation cannot be excluded by our observations and that an abundance analysis, particularly of nitrogen in the shell, would be required to exclude or confirm a classical nova origin for the nebula.

In both systems, the infrared emission consistently marks the most extended component of the bow shock, whereas the [O III] bright optical emission is confined to a smaller bow-shaped region closer to the central system. This spatial ordering mirrors the layered morphology identified in BZ Cam and suggests that a similar stratification is present in RXJ0528+2838 and V341 Ara (Figure 2), even though the absence of FUV data prevents a direct detection of the shocked-wind cavity.

4. Discussion and Conclusions

We have used archival UV, optical, and infrared imaging to test whether bow shocks around CVs exhibit the two-shock structure predicted by wind–ISM interaction theory. The combined multiwavelength data for BZ Cam, V341 Ara, and RXJ0528+2838 reveal a consistent, layered morphology that

[9] https://github.com/HC-Hwang/wise_light_curves

naturally maps onto the expected terminal-shock, shocked-wind, and forward-shock zones.

All three systems show an outer infrared arc detected in unWISE W2, reported here for the first time in each object. This infrared-bright rim marks the most extended component of the bow shock and traces the compressed, swept-up material at or near the forward shock. Its appearance in W2 but not W1 indicates emission from relatively cool dust concentrated in the outer boundary of the shocked region.

In BZ Cam the region interior to the infrared rim is filled with FUV emission and faint Hα, consistent with a hot, low-density shocked-wind cavity between the terminal and forward shocks. Although FUV data are not available for V341 Ara or RXJ0528+2838, their morphologies show the same intermediate layer in the form of a faint, extended Hα envelope.

The compact Hα+[O III] arcs in all systems correspond to the inner bow shock. This structure is the same feature that has traditionally been identified as the bow shock in previous studies, but our results suggest it corresponds to the terminal/reverse shock front rather than the forward shock as previously assumed.

Taken together, these results show that CV bow shocks are fundamentally multilayered structures: an inner terminal-shock front producing the bright optical arc, a hot shocked-wind cavity that can emit strongly in the FUV, and an outer forward-shock/H II boundary traced by infrared-emitting dust. The presence of this same layered structure in both disk-bearing nova-likes and in a diskless polar suggests that the observed morphology is governed primarily by the physics of the wind–ISM interaction, independent of the specific outflow-launching mechanism.

Future spatially resolved UV and infrared spectroscopy will be essential for determining the physical conditions within each layer and for constraining the long-term mass-loss histories of accreting WDs.

Acknowledgments

This work was supported by the Polish National Science Centre (NCN) grant 2024/55/D/ST9/01713. S.S. acknowledges support by the Science and Technology Facilities Council (STFC) grant ST/X001075/1.

This research made use of APLpy, an open-source plotting package for Python (T. Robitaille & E. Bressert 2012). This work has made use of data from the European Space Agency (ESA) mission Gaia (https://www.cosmos.esa.int/gaia), processed by the Gaia Data Processing and Analysis Consortium (DPAC; https://www.cosmos.esa.int/web/gaia/dpac/consortium). Funding for the DPAC has been provided by national institutions, in particular the institutions participating in the Gaia Multilateral Agreement.

Data Availability

This work is based exclusively on archival data. No new observations were obtained by the authors. Some of the data presented in this Letter were obtained from the Mikulski Archive for Space Telescopes (MAST) at the Space Telescope Science Institute. The specific observations analyzed can be accessed via doi:10.17909/cxk9-jt29.

Facilities: WISE, GALEX, VLT:Yepun

Software: aplpy (T. Robitaille & E. Bressert 2012).

Appendix
WISE Knots in the BZ Cam Outer Shell

The W2 arc of BZ Cam contains multiple compact clumps coincident with WISEA entries (WISEA identifiers). Using catalog photometry (R. M. Cutri et al. 2021), we identified 11 such clumps lacking obvious optical counterparts, of which 4 have W1 – W3 measurements and only upper limits in W4, and the remaining 7 are detected only in W1 and W2. For the 4 three-band clumps we fitted simple blackbodies by sampling the blackbody parameter space with a Markov Chain Monte Carlo method, obtaining characteristic temperatures of ∼500–600 K (Appendix Figure 4). Multiepoch W1/W2 photometry following H.-C. Hwang & N. L. Zakamska (2020) shows no significant variability within the uncertainties.

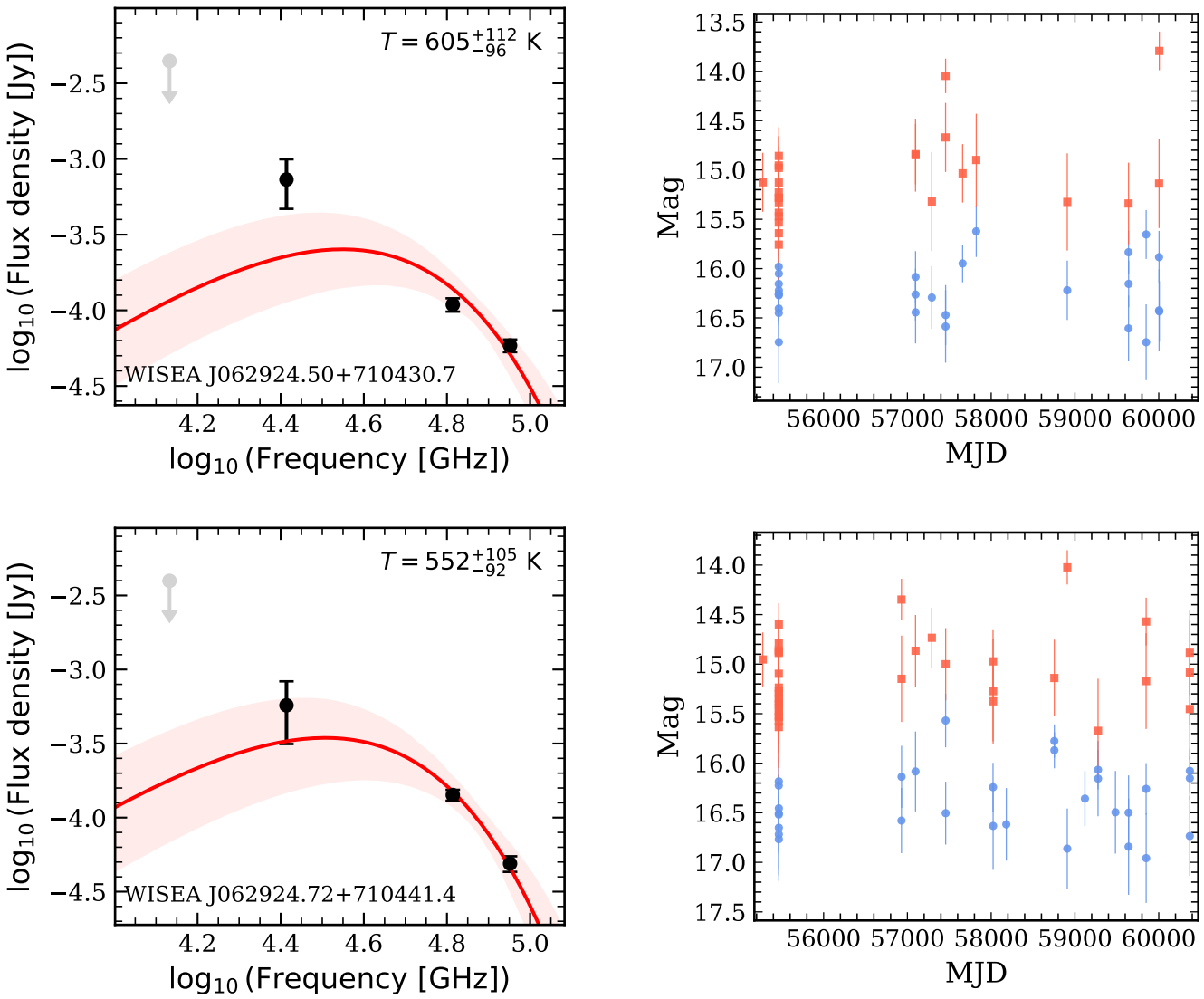

Figure 4. SEDs (left) and W1/W2 light curves (right) for representative WISEA clumps on the BZ Cam outer shell. Red curves show blackbody fits; shaded regions indicate fit uncertainties.

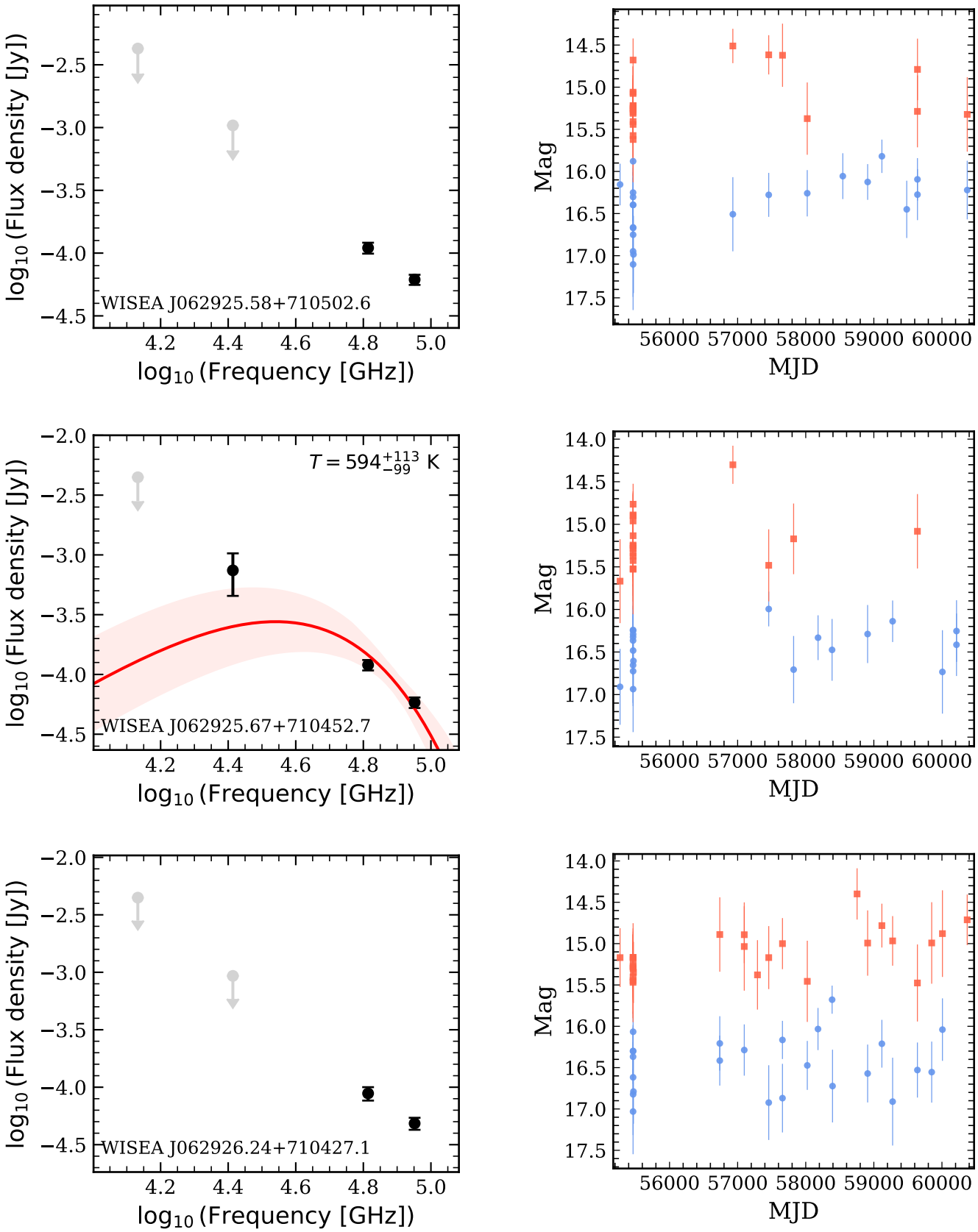

Figure 4. (Continued.)

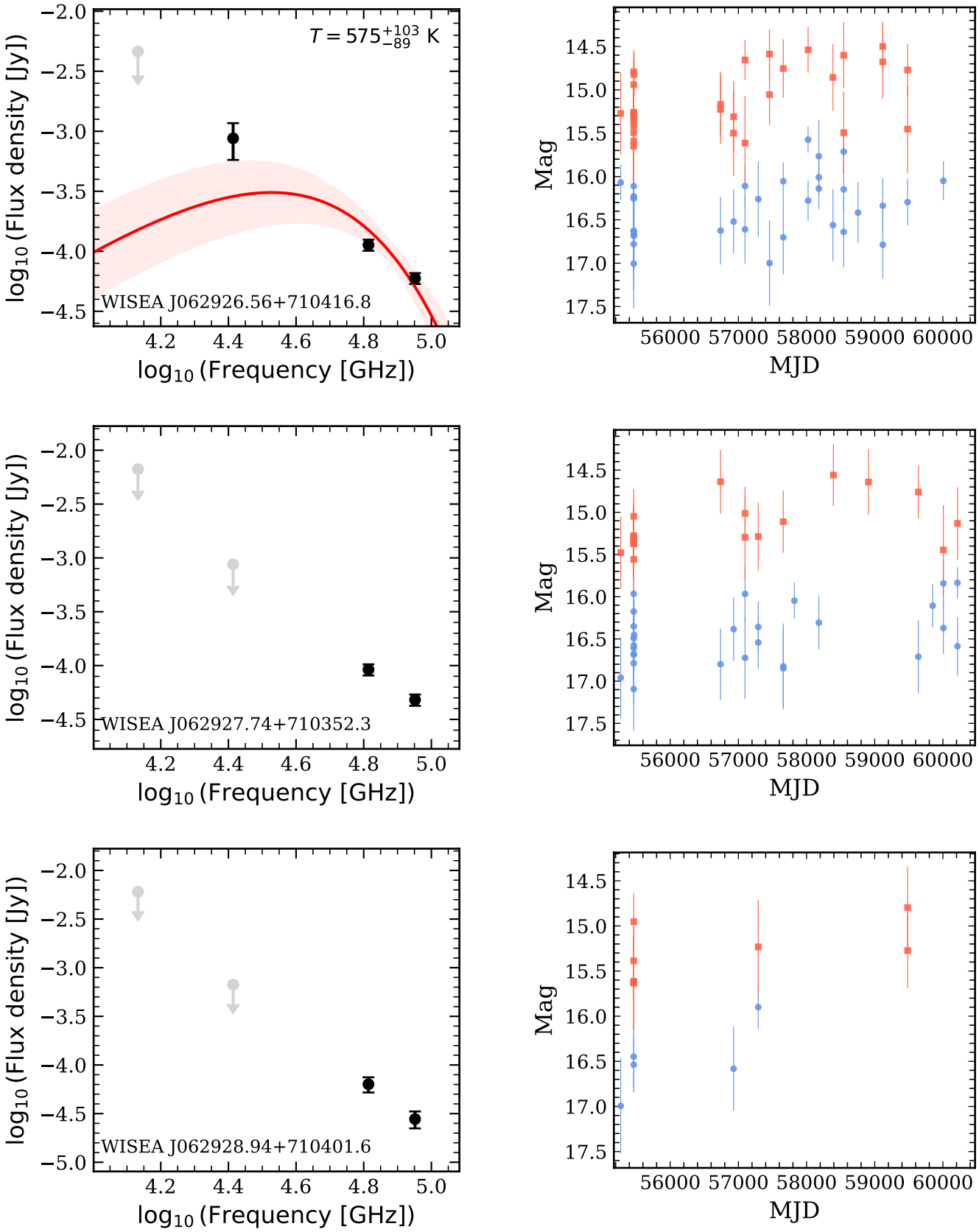

Figure 4. (Continued.)

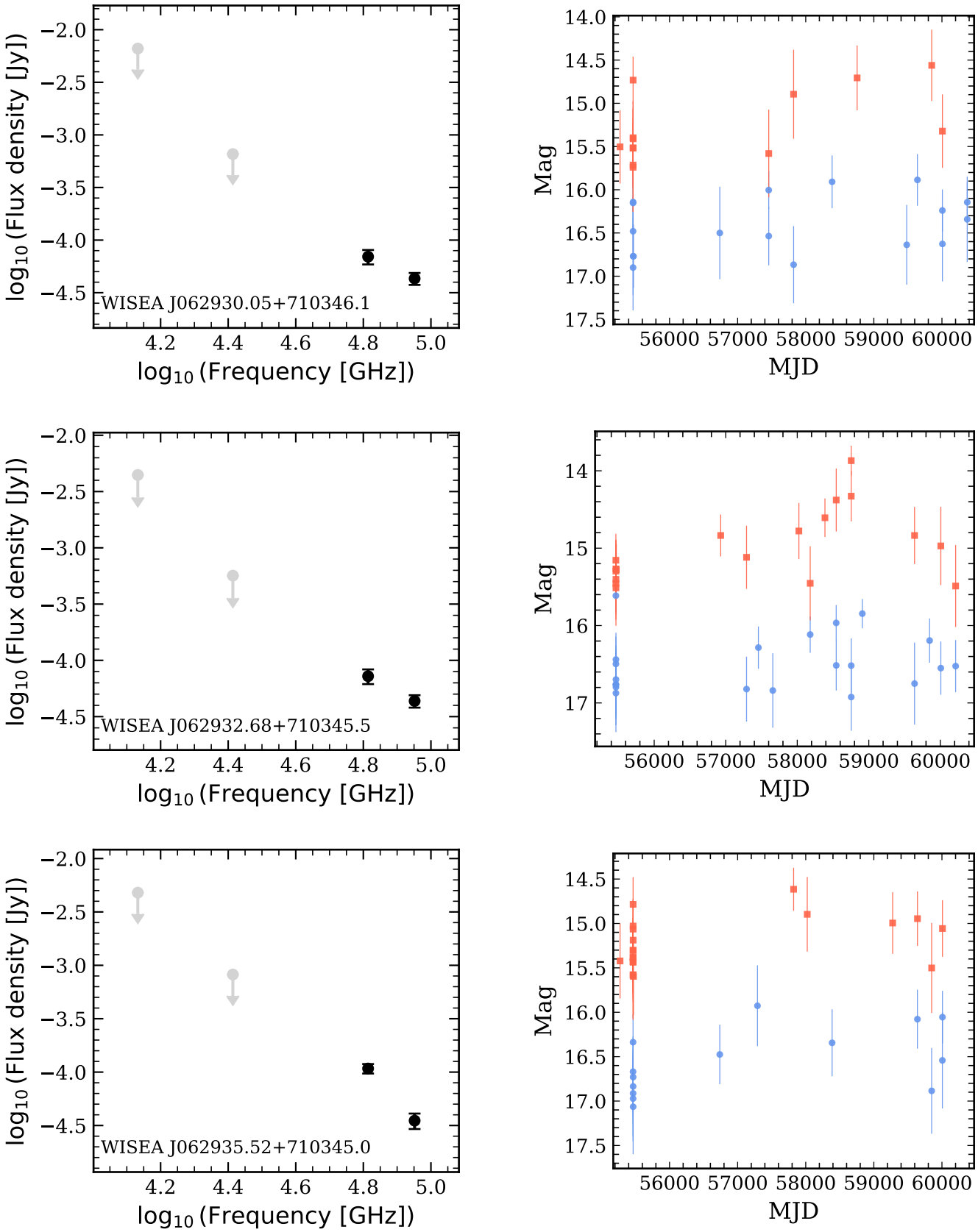

Figure 4. (Continued.)

ORCID iDs

Krystian Iłkiewicz https://orcid.org/0000-0002-4005-5095
Christian Knigge https://orcid.org/0000-0002-1116-2553
Simone Scaringi https://orcid.org/0000-0001-5387-7189
Noel Castro Segura https://orcid.org/0000-0002-5870-0443
Santiago del Palacio https://orcid.org/0000-0002-5761-2417
Martina Veresvarska https://orcid.org/0000-0002-0146-3096

References

Barkov, M. V., Lyutikov, M., & Khangulyan, D. 2019, MNRAS, 484, 4760
Bond, H. E., Carter, C., Coles, E., et al. 2025, PASP, 137, 114301
Bond, H. E., & Miszalski, B. 2018, PASP, 130, 094201
Bonnarel, F., Fernique, P., Bienaymé, O., et al. 2000, A&AS, 143, 33
Castro Segura, N., Knigge, C., Acosta-Pulido, J. A., et al. 2021, MNRAS, 501, 1951
Cutri, R. M., Wright, E. L., Conrow, T., et al. 2021, yCat: AllWISE Data Release (Cutri+ 2013), VizieR On-line Data Catalog: II/328. Originally published in: IPAC/Caltech (2013),
Gaia Collaboration, Vallenari, A., Brown, A. G. A., et al. 2023, A&A, 674, A1
Greiner, J., Tovmassian, G., Orio, M., et al. 2001, A&A, 376, 1031
Hernández Santisteban, J. V., Echevarría, J., Zharikov, S., et al. 2019, MNRAS, 486, 2631
Hollis, J. M., Oliversen, R. J., Wagner, R. M., & Feibelman, W. A. 1992, ApJ, 393, 217
Hwang, H.-C., & Zakamska, N. L. 2020, MNRAS, 493, 2271
Iłkiewicz, K., Scaringi, S., de Martino, D., et al. 2026, NatAs, Advanced Online Publication
Krautter, J., Klaas, U., & Radons, G. 1987, A&A, 181, 373
Lang, D. 2014, AJ, 147, 108
Morrissey, P., Conrow, T., Barlow, T. A., et al. 2007, ApJS, 173, 682
Robitaille, T., & Bressert, E. 2012, APLpy: Astronomical Plotting Library in Python, Astrophysics Source Code Library, ascl:1208.017
Sanchez-Bermudez, J., Schödel, R., Alberdi, A., et al. 2014, A&A, 567, A21
Zemko, P., Orio, M., Mukai, K., & Shugarov, S. 2014, MNRAS, 445, 869